Acta Crystallographica Section A
Foundations of Crystallography
ISSN 0108-7673

Received 16 September 2009
Accepted 24 December 2009

Time-resolved synchrotron diffraction and theoretical studies of very short-lived photo-induced molecular species

Philip Coppens,[a]* Jason Benedict,[a] Marc Messerschmidt,[a]‡ Irina Novozhilova,[a] Tim Graber,[b] Yu-Sheng Chen,[b] Ivan Vorontsov,[a]§ Stephan Scheins[a] and Shao-Liang Zheng[a]¶

[a]Chemistry Department, University at Buffalo, State University of New York, Buffalo, NY 14260-3000, USA, and [b]CARS, University of Chicago, Chicago, IL 60637, USA. Correspondence e-mail: coppens@buffalo.edu

Definitive experimental results on the geometry of fleeting species are at the time of writing still limited to monochromatic data collection, but methods for modifications of the polychromatic Laue data to increase their accuracy and their suitability for pump–probe experiments have been implemented and are reviewed. In the monochromatic experiments summarized, excited-state conversion percentages are small when neat crystals are used, but are higher when photoactive species are embedded in an inert framework in supramolecular crystals. With polychromatic techniques and increasing source brightness, smaller samples down to tenths of a micrometre or less can be used, increasing homogeneity of exposure and the fractional population of the excited species. Experiments described include a series of transition metal complexes and a fully organic example involving excimer formation. In the final section, experimental findings are compared with those from theoretical calculations on the isolated species. Qualitative agreement is generally obtained, but the theoretical results are strongly dependent on the details of the calculation, indicating the need for further systematic analysis.

1. Introduction

Like the concepts 'small' and 'large', 'time-resolved' has a most ambiguous meaning. It can refer to processes which take forever (plate tectonics), hours, microseconds, femtoseconds and even attoseconds, all having in common that the time is the significant variable. In molecular science, solid state reactions may take hours, but the initial process on triggering the reaction may be over in femtoseconds. Studies of all stages are needed for a full understanding of such processes. The drive towards the study of faster processes is supported by shorter and shorter pump and probe pulse lengths available from novel lasers and at the new fourth-generation light sources, respectively. Our current knowledge of what is happening immediately after initiation of a reaction is modest at best but crucial for the understanding of what happens next. What do we want to learn, how fast are the processes we want to examine or how short are the lifetimes of the species we have to look at?

This review will concentrate on atomic resolution species at microsecond, nanosecond and picosecond lifetimes. The first include thermally equilibrated excited triplet states which are usually highly reactive and intermediates in photochemical reactions, whereas excited singlet states typically have lifetimes of nanoseconds and picoseconds, and even less. Processes which occur immediately on excitation such as Franck–Condon transitions and electron injection from adsorbents on semiconductor substrates produce species which are typically of femtosecond duration. Their geometry is becoming accessible with the new free-electron lasers, and by time-resolved electron diffraction studies discussed elsewhere in this issue.

2. Methods

The ratio of the repeat frequencies of the laser-pump and photon-probe pulses which are to be synchronized in time-resolved studies is a fundamental parameter in the experimental design. At synchrotron sources very high pulse-repeat rates of several MHz are achieved. At the Advanced Photon Source (APS) the orbit time is 3.68 μs, which means that even with a single bunch in the ring the pulse repeat frequency is 271.554 kHz, and 24 times as large in the standard mode with 24 equidistant bunches. Sufficiently powerful lasers, on the

‡ Current address: SLAC, National Laboratory at Stanford University, Stanford, CA 94305, USA.

§ Current address: Department of Biochemistry and Molecular Biophysics, University of Arizona, Tucson, AZ 85721, USA.

¶ Current address: Chemistry Department, Harvard University, USA.

other hand, are limited to repeat rates of 15–25 kHz, so that a very large fraction of the synchrotron photons must be discarded, and high-speed choppers must be used to select a subset of the X-ray pulses. The result is that even at intense synchrotron sources experiments may be effectively flux-limited, especially when monochromatic beams are used. In that case a stroboscopic technique can be used in which pump–probe cycles are repeated and accumulated on a single detector frame until a sufficient level of counting statistics is reached. But this approach is only feasible when the process being studied is time-reversible on a short timescale, as is typically the case for short-lived molecular excited states in crystals. Polychromatic experiments using larger bandwidths from undulators or multilayers can lead to improvements in flux by factors of 1000 or more, and make it possible to collect data with a single synchrotron pulse. If the laser pulse is followed by a single X-ray pulse, the time resolution is determined by the largest width of the pump and the probe pulses. Thus, with femtosecond lasers the time resolution is determined by the width of the synchrotron pulse which is typically ~50–160 ps, depending on the filling pattern of the ring, although, at a significant expense of flux, femtosecond pulses can be generated using time-slicing methods (Schoenlein *et al.*, 2000). Recently, a method for generating picosecond-length pulses without a large loss in intensity has been proposed (Guo *et al.*, 2007).

2.1. The monochromatic approach

Monochromatic experiments are based on a narrow bandwidth X-ray beam. If a silicon (111) monochromator is used, the bandwidth $\Delta E/E$ is typically 10^{-4}, 0.01% or 1 eV at 10 keV. Depending on the spacing of the diffraction spots in reciprocal space, a larger bandwidth, such as that available from multilayers, can be used without crossing the boundary to Laue diffraction. High-resolution multilayers, with alternating layers of composition Mo/B_4C and W/B_4C, having bandwidths of 0.2–2% have been installed at several sources, including CHESS (Kazimirov *et al.*, 2006). They reportedly can deliver a 100 times increase in intensity even before focusing optics are applied, and have significant advantages in time-resolved studies.

In the stroboscopic experiment the pump–probe cycle is repeated until counting statistics reach an adequate level. Because of the use of only a fraction of the X-ray photons, multibunch X-ray pulse trains must be used, thus limiting time resolution. With a typical X-ray pulse spacing of hundreds of nanoseconds (153.4 ns at APS in 24-bunch mode), this means that in a multibunch experiment time resolution will be limited to the microsecond range. At this resolution powerful high-rep-rate Nd:YAG and Nd:vanadate lasers with pulse lengths of 10–70 ns can be used as pump sources. The advantage of this is that longer pulses with lower peak power induce significantly less laser damage in the sample.

The length of the interrogating X-ray probe pulse train can be varied by adjusting the beam chopper's rotation speed and slot opening (Gembicky & Coppens, 2007) and must be commensurate with the lifetime of the state being studied. The ratio $N(t)/N(0)$ of the average number of excited molecules in the sample relative to the number of molecules initially excited is shown for an exponential decay curve as a function of t/τ (t = time, τ = lifetime of the excited species) in Fig. 1. An X-ray exposure length of one lifetime gives an average population in the sample of ~60% of the molecules initially excited.

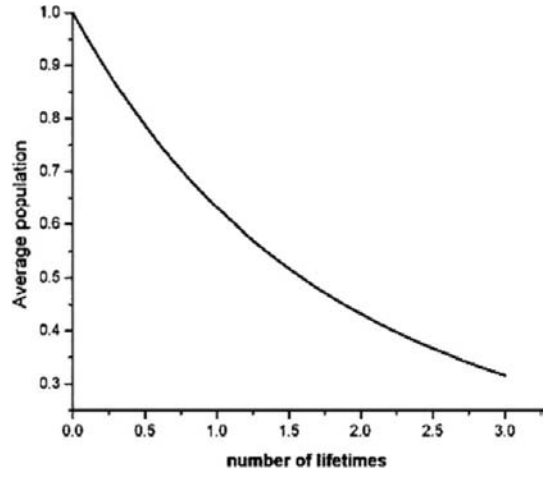

Figure 1
Average population as a function of X-ray probe duration.

To eliminate long-term fluctuation owing to factors such as beam decay and crystal deterioration, the laser-on and laser-off measurements at each setting are made sequentially. In our monochromatic experiments the least-squares refinement of the observations is based on the response ratios η, defined by

$$\eta = \frac{I_{ON} - I_{OFF}}{I_{OFF}} = \frac{I_{ON}}{I_{OFF}} - 1 \equiv R - 1, \qquad (1)$$

in which R is the I_{ON}/I_{OFF} ratio. A modified analysis based on R is applied to polychromatic Laue data, as described in the next section. For a more detailed description of the stroboscopic technique the reader is referred to an earlier publication (Coppens *et al.*, 2005).

2.2. Laue studies at atomic resolution

Experiments were performed at the BIOCARS beamline 14-ID at APS (Graber *et al.*, 2009). Limited-bandwidth 'pink' Laue studies make use of one of the harmonics emanating from an undulator. The spectrum of the first harmonic of the U23 undulator at beamline 14-ID of BioCARS, tuned to a peak wavelength of 16 keV, is shown in Fig. 2 (blue curve). The spectral curve has a FWHM of about 1 keV, *i.e.* about 6% of the energy.

2.2.1. Wavelength scaling. The undulator beam at 14-ID is very intense and allows collection of data on a small crystal with a single pulse of the synchrotron (Fig. 3) which shows its suitability for picosecond timescale time-resolved diffraction. But the spectrum is quite asymmetric (Fig. 2, blue curve) and has a long tail on the long-wavelength side. This raises the question of how intensities collected at different wavelengths

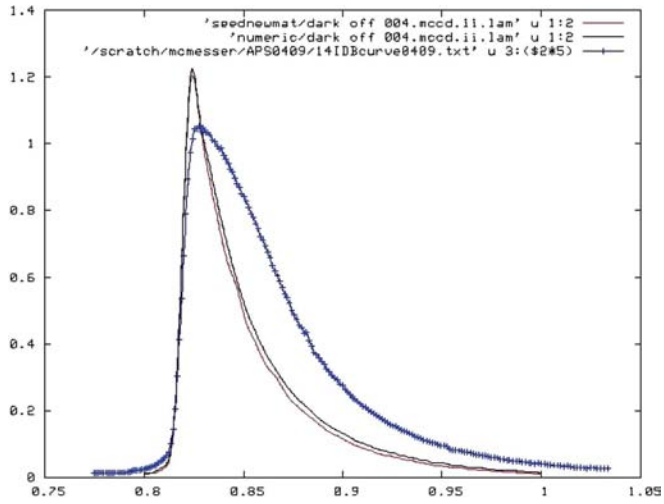

Figure 2
Experimental spectrum (blue) *versus* wavelength normalization (λ) curve.

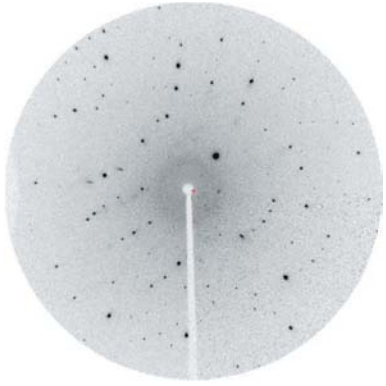

Figure 3
A single-pulse diffraction pattern for a $(CuCl)_4$ cubane complex.

can be combined. The solution applied in macromolecular crystallography is to derive a 'λ' curve from the scaling of equivalent reflections collected originating from the scattering of different wavelengths (Helliwell *et al.*, 1989; Ren & Moffat, 1995). This method is applicable to crystals with smaller, but not too small, unit cells, as illustrated in Fig. 2 (purple and black curves), in which the measured spectral distribution is compared with the 'λ' curve for a moderate unit cell crystal. The spectral and λ curves are not identical as the latter will include effects such as the wavelength dependence of absorption in the crystal and detector response. But the fitted curves, shown in purple and black for different numbers of Chebyshev polynomial fitting functions, show fluctuations owing to the fitting which limit the accuracy of the processed intensity. We have therefore developed an alternative procedure which eliminates the wavelength dependence. In the RATIO method, the I_{hkl}(ON)/I_{hkl}(OFF) ratios are calculated and averaged over symmetry-equivalent and repeated measurements (Coppens *et al.*, 2009). A reference monochromatic data set $I_{OFF}(hkl)$ is then collected at a conventional

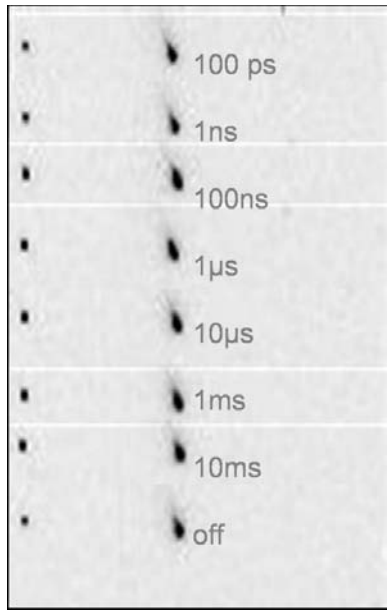

Figure 4
Spot shape as a function of the delay time between the pump and probe pulses. The weaker spot on the left expands less than the spot on the right.

diffractometer and used to calculate the 'ON' structure factors using $I_{ON}(hkl) = I_{OFF}(hkl)R(hkl)$, where R is the ratio of the ON and OFF intensities obtained from the synchrotron experiment.

2.2.2. Spot-shape variation and integration of Laue spots. A striking observation of picosecond time-resolved diffraction is the variation of the spot shape with the time delay between the pump and probe pulses. When intensities are collected in a series of runs at different delays, a dramatic reversible extension of the spot shape is observed. The size and shape variation of two spots collected on a crystal of $Cu_4Cl_4(dpmp)_4$ [dpmp = 2-(diphenylmethyl)pyridine] is shown in Fig. 4. The process is reversible; after 10 ms the original spot shape has almost been recovered, and is attributed to the progress of a light-induced shockwave through the crystal. But the shape of the spots makes them poorly suitable for the profile-fitting procedure commonly used in the integration of Laue data. We have therefore used the earlier developed seed-skewness method. It does not depend on a learned profile, but is based on a search for the minimum in the skewness of the intensity distribution of the pixels assigned to the background upon increasing size of a seed growing outwards from the central peak position (Bolotovsky & Coppens, 1997). An example of a spot boundary calculated with the program *LaueGUI* (Messerschmidt & Tschentscher, 2008) using the seed-skewness method is shown in Fig. 5. The method leads to a significant improvement in R_{merge} compared with macromolecular integration programs used in earlier studies.

2.3. Selection of crystal size

For a successful experiment the uniformity of the illumination should be optimized throughout the sample. This is not a trivial task as the molecular concentration in neat crystals

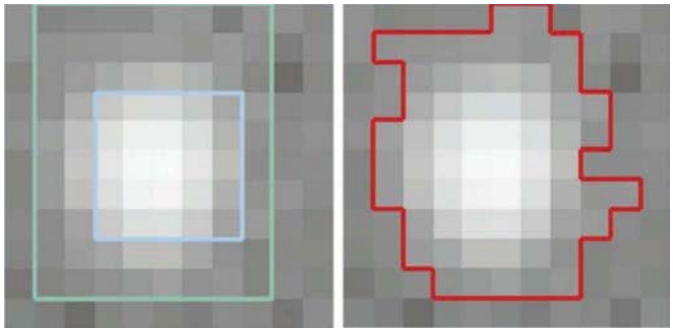

Figure 5
Pixel intensities (left) and results of the seed-skewness analysis of the spot shape (right).

is high. For example, for a concentration of 5 mol l^{-1} and an extinction coefficient ε of 100 m^2 mol^{-1}, the transmission through a 10 μm crystal is only 10%, as illustrated in Fig. 6. Several possible strategies can be adopted to increase the homogeneity of the light exposure:

(i) The molecules can be inserted into a photochemically inert medium using the techniques of crystal engineering, thus achieving solid state dilution while retaining the periodic nature of the medium.

(ii) The wavelength can be selected to correspond to a tail of the absorption band in order to reduce the extinction coefficient (Abdelmoty *et al.*, 2005; Enkelmann & Wegner, 1993).

(iii) Two-photon absorption can be used. It allows use of photons with a longer wavelength not corresponding to the absorption band (Benedict & Coppens, 2009). But as the cross sections are small, it is probably not applicable to single-pulse experiments in which a significant number of molecules must be excited in a picosecond time span.

(iv) Crystal size must be minimized. This is the most obvious way to ensure even exposure throughout the sample, but it increases the need for space stability of the probing X-ray beam. It has the added advantage that external cooling will be more effective, thus reducing possible temperature increases on laser-light exposure.

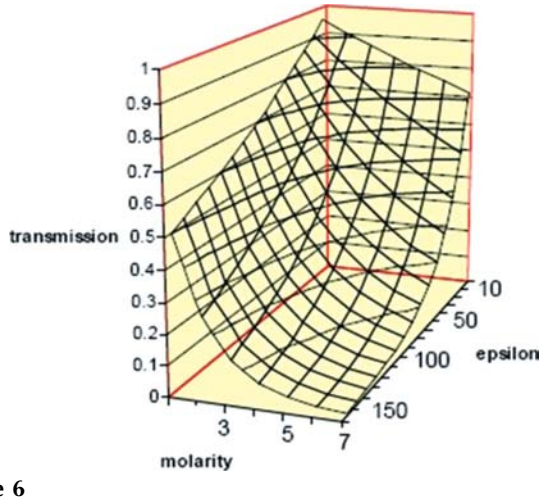

Figure 6
Transmission for a 10 μm crystal as a function of the extinction coefficient ε (in m^2 mol^{-1}) and the molarity of the crystal.

2.4. The scattering model

If the excited-state molecules are randomly distributed in the crystal, the elastic diffraction pattern will be that of the space-averaged electron density distribution, given by

$$F_{ON}(hkl) = (1 - P)F_{ON,\,ground}(hkl) + PF_{ON,\,excited}(hkl), \quad (2)$$

in which P is the excited-state population, and $F_{ON,\,ground}(hkl)$ and $F_{ON,\,excited}(hkl)$ are the structure factors for the ground- and excited-state components in the exposed crystal. The difference in the intensities between this random distribution model and those calculated with the cluster formation model, which leads to domain formation, is large (Vorontsov & Coppens, 2005). The latter is valid when the excitation process is much more likely to occur adjacent to already converted molecules. If significant unit-cell changes occur, and domains are sufficiently large, the latter model will lead to new diffraction spots, which have not been observed in any of our experiments, the results of which have been well fitted by expression (2). But kinetic analysis of the [2+2] dimerization of α-cinnamic acid indicates that the mechanism of the photo-induced dimerization reaction is intermediate between that of a random distribution and the existence of growing nuclei (Benedict & Coppens, 2009), indicating that intermediate situations may occur when chemical reactions are considered. For nuclei much smaller than the coherence length of X-rays in the crystal, the random distribution model will still be valid.

3. Selected experimental results

3.1. Excited states of molecules in neat crystals

3.1.1. Molecular contraction. We have studied the excitation of a number of transition metal metal-organic complexes in neat crystals. Several of these demonstrate the effect of excitation of an electron from the highest orbital of a complete atomic electron shell. In the binuclear complexes of Pt, Rh and Cu the excitation leads to a decrease of the metal–metal bond length as an electron is promoted from an antibonding d orbital to a weakly bonding $p\sigma$ orbital with a higher principal quantum number.

The first diffraction study (Kim *et al.*, 2002), at 17 K with 355 nm excitation, was performed on $(TEA)_3H[Pt_2(pop)_4]$ [pop = pyrophosphite, $(H_2P_2O_5)^2$, TEA = tetraethyl-ammonium]. The observed bond shortening of 0.28 (9) Å was within the experimental error equal to values determined spectroscopically from analyses of the IR spectra in crystals (0.21 Å) (Rice & Gray, 1983) and Raman spectra of an aceto-nitrile solution (0.225 Å) (Leung *et al.*, 1999). The value has since been confirmed by a value of 0.23 (4) Å in a second diffraction experiment (Ozawa *et al.*, 2003), and more recently by scattering measurements on an aqueous solution [0.24 (6) Å] (Christensen *et al.*, 2009) and a time-resolved EXAFS study [0.31 (5) Å] (van der Veen *et al.*, 2009). The latter study also yielded, for the first time, a value for the

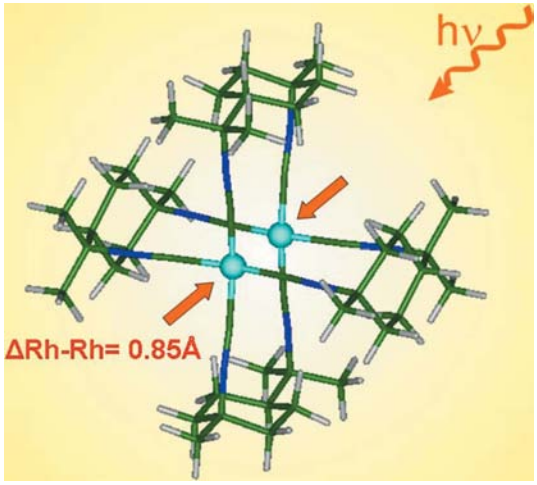

Figure 7
Contraction of the Rh—Rh distance in the excited triplet state of Rh_2(1,8-diisocyano-*p*-menthane)$_4^{2+}$ (Coppens *et al.*, 2004).

lengthening of the Pt—P bonds [0.010 (6) Å] in agreement with the results of theoretical calculations (Novozhilova *et al.*, 2003). The experimental Pt—Pt contraction was used to test a series of theoretical excited-state calculations, the results of which depend strongly on the choice of relativistic treatment of the platinum atom (Novozhilova *et al.*, 2003), as discussed further below.

A second study was performed on crystals of [Rh_2(1,8-diisocyano-*p*-menthane)$_4$](PF_6)$_2$·CH_3CN (Fig. 7) which at 23 K has an excited-state lifetime of 11.7 μs with an emission maximum at 660 nm. A very large Rh—Rh contraction of 0.86 (5) Å was observed on excitation of the ion to its triplet state (Coppens *et al.*, 2004). But the small excited-state populations achieved, 1.9 and 2.5% in two successive experiments, prevented determination of the shifts of the lighter atoms in this study.

{[3,5-(CF_3)$_2$pyrazolate]Cu}$_3$ crystallizes in stacks of parallel molecules in the monoclinic crystal (Fig. 8). Time-resolved diffraction showed that on excitation an intermolecular process occurs with a contraction of one interstack Cu—Cu distance by 0.56 Å, from 4.020 (1) to 3.46 (1) Å (Vorontsov *et al.*, 2005). The Cu3 triangles tilt only slightly (by 0.9°) on photoexcitation. The interplanar spacing of two center-of-symmetry related trimers in the stack is reduced by 0.65 Å from 3.952 (1) to 3.33 (1) Å. The geometry change corresponds to a dimerization and not a chain compression, as the second interplanar distance is increased from 3.610 (1) to 3.91 (1) Å. In other words, the shorter interplanar distance increases, while the longer spacing decreases on excitation, an unexpected result of the study.

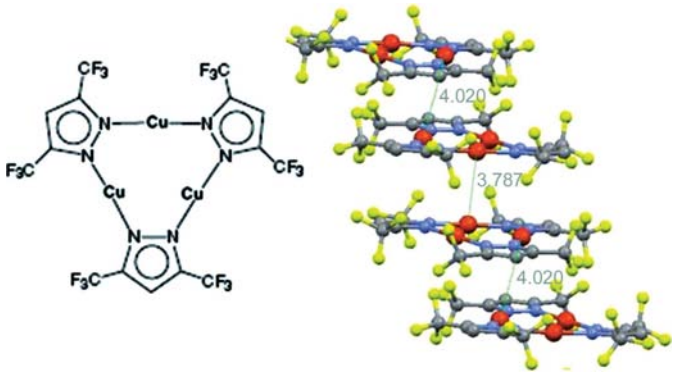

Figure 8
Left: the {[3,5-(CF_3)$_2$pyrazolate]Cu}$_3$ trimer. Right: packing of the molecules in the crystal. Distances shown are between atoms.

3.1.2. Molecular distortion on excitation of a photosensitizer dye. The photosensitizer dye [Cu^I(dmp)(dppe)][PF_6] [dmp = 2,9-dimethyl-1,10-phenanthroline, dppe = 1,2-bis(diphenylphosphino)ethane] is a prototype of molecules with relatively long-lived excited states generated by MLCT (metal-to-ligand charge transfer) or LLCT (ligand-to-ligand charge transfer) processes. Such molecules are promising low-cost alternatives to Ru complexes for functionalizing TiO_2 in photovoltaic cells (Bessho *et al.*, 2008). The four bonds around the Cu atom are expected to flatten towards the square-planar configuration typical for Cu^{II}, although this motion is restricted by the 2,9 methyl substitution in the phenanthroline ring. The most pronounced shifts on excitation occur for the Cu atoms, which move by 0.26 (2) and 0.28 (2) Å for the two independent molecules in the asymmetric unit, respectively. The attached phosphorous atoms move in the same direction (Vorontsov *et al.*, 2009). The distortions are illustrated in Fig. 9 for one of the two independent molecules.

The expected flattening is very small, in part because of the 2,9 methyl substituents, but also because of space restrictions in the crystal. Comparison with theory shows that the distortions are expected to be larger for the isolated molecule, as discussed in the theoretical section of this review. Such restraints are expected to be significantly reduced in host–guest supramolecular crystals in which extra space is often available in the cavity in which the guest molecules are located.

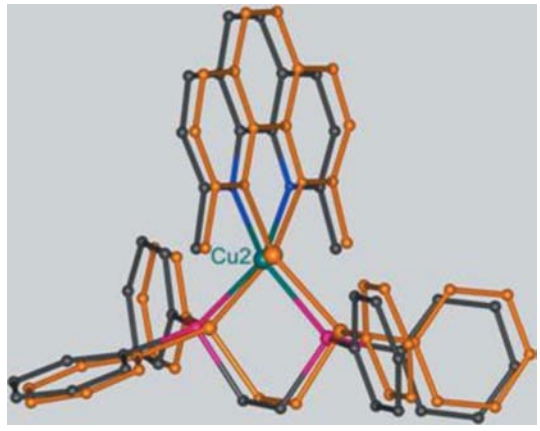

Figure 9
Excited-state geometry of one of the independent molecules (orange) superimposed on the ground state of the complex (Cu: green; C: black; P: purple; N, blue). The change in rocking distortion and the displacement of aromatic rings from their ground-state planes on excitation are evident. [Reprinted with permission from Vorontsov *et al.* (2009). Copyright 2009 American Chemical Society.]

3.2. Excited states of guest species in supramolecular crystals

The use of supramolecular solids opens a whole new range of possibilities in the photochemistry of molecules in solids. A great variety of solids can be synthesized, even with one guest molecule (Ma & Coppens, 2003; Zheng *et al.*, 2006). Spectroscopists have for a long time used rigid glasses as a means to isolate individual molecules and reduce the concentration of the active species in the medium. Unlike rigid glasses, host–guest supramolecular solids are periodic. Structural stability is provided by the host components, so that crystal breakdown on molecular change is less likely to occur, and the molarity of the guest molecules is reduced in comparison with neat crystals. However, energy transfer from the excited guest to the host molecules can lead to emission quenching owing to rapid decay of the excited-state populations. A mismatch of energy levels and host and guest molecules can be engineered by selecting host species without extended conjugated systems. This will greatly reduce energy transfer and thereby extend the excited-state lifetime of the guest molecules (Zheng & Coppens, 2005*a*).

3.2.1. Molecular contraction of a dinuclear Cu^{I} species stabilized in a supramolecular framework. Calculations show that the dimeric cationic species $[Cu(NH_3)_2]_2^{++}$ is not stable with respect to dissociation (Carvajal *et al.*, 2004), nor does it form salts with isolated anions. However, it exists as a guest in the anionic framework formed by $[H_2THPE]^-$ [H_3THPE = tris(hydroxyphenyl)ethane] (Fig. 10) in which it is stabilized by hydrogen bonding to the host lattice. Time-resolved diffraction of its 52 µs (17 K) excited triplet state and subsequent analysis leads to a Cu—Cu bond shortening from 3.025 (1) to 2.72 (1) Å on excitation (Coppens *et al.*, 2006). In addition, a 7° rotation of the molecular ion occurs, as illustrated in Fig. 11.

This compound, the $[Pt_2(pop)_4]^{4-}$ and $[Rh_2(1,8\text{-diisocyano-}p\text{-menthane})_4]^{2+}$ ions, and the $\{[3,5\text{-}(CF_3)_2\text{pyrazolate}]Cu\}_3$ complex have in common that on excitation an electron is ejected from an antibonding orbital and inserted into a weakly bonding orbital with a higher quantum number leading to a molecular contraction on excitation. The HOMO and LUMO orbitals for $[Rh_2(1,8\text{-diisocyano-}p\text{-menthane})_4]^{2+}$ are shown below in Fig. 16.

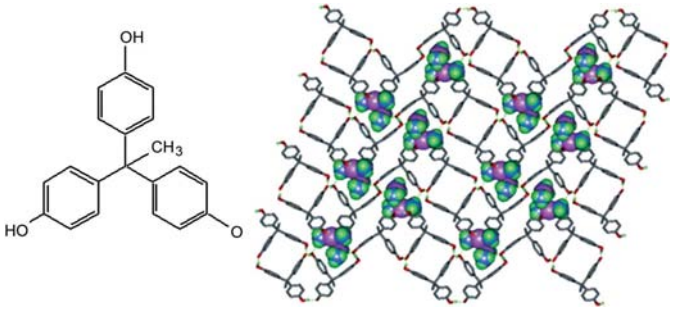

Figure 10
Left: the THPE molecule. Right: the $[Cu(NH_3)_2]_2^{++}$ cation embedded in an anionic framework of $[H_2THPE]^-$ (Zheng *et al.*, 2005). Copyright Wiley-VCH Verlag GmbH & Co. KGA. Reproduced with permission.

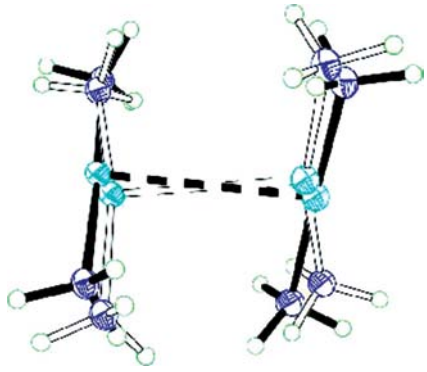

Figure 11
Bond shortening and molecular rotation of the $[Cu(NH_3)_2]_2^{++}$ ion on excitation. Filled lines: ground state. Open broken lines: excited state.

3.2.2. Excimer formation on exposure of a dimeric complex embedded in a supramolecular solid. The aromatic molecule xanthone is a prototype of molecules such as pyrene and anthracene, which can form short-lived excited-state dimers. They have been studied extensively by spectroscopic means (East & Lim, 2000; Forster, 1965; Forster & Kasper, 1954; Lim, 1987, 2002; Lim *et al.*, 1987), but have not been observed by diffraction methods until the advent of time-resolved crystallography. When co-crystallized with HECR (hexaethyl calix[6]resorcinarene), a solid of composition HECR-2xanthone-6MeOH is formed in which xanthone shows an excited-state lifetime of 5.56 µs (Zheng & Coppens, 2005*b*). X-ray analysis indicates that, in contrast to xanthone in CECR (C-ethylcalix[4]resorcinarene) in which it is included as a monomer, the xanthone molecules in HECR form a π-stacked dimer (Fig. 12).

The stroboscopic time-resolved experiments indicate a contraction of the interplanar spacing by 0.25 (3) Å, from 3.39 to 3.14 Å, as expected for excimer formation. The experi-

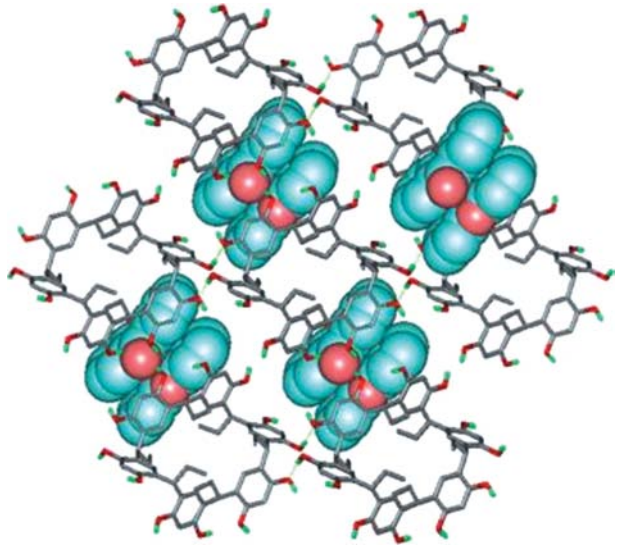

Figure 12
Three-dimensional view of HECR-2xanthone-6MeOH containing dimeric xanthone (Zheng & Coppens, 2005*b*). Copyright Wiley-VCH Verlag GmbH & Co. KGA. Reproduced with permission.

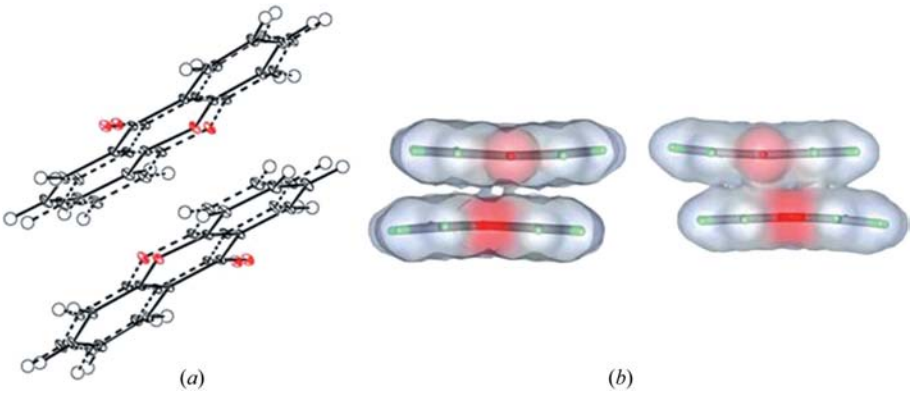

Figure 13
Change in the xanthone dimer on excimer formation. (*a*) Full lines: ground state; broken lines: excited state. (*b*) Sideways view. Note the relative offset of the molecular planes. [Coppens *et al.* (2006) – Reproduced by permission of the Royal Society of Chemistry.]

mentally measured contraction is accompanied by a relative lateral shift of the molecular planes of 0.24 Å (Fig. 13).

The experimental excited-state populations are found to be 8 and 13% in two successive experiments, the second with increased power in the laser beam. As in the Cu dimer, in which a conversion of 9.1% was reached, this is larger than 2–6% excited-state populations achieved in our experiments with neat crystals, a result attributed to the improved photon/photoactive-molecule ratio in the supramolecular crystals.

4. Parallel theoretical calculations

Parallel theoretical calculations are a key complement to time-resolved diffraction studies. How well are the experimental results reproduced by theory? Can they be used for calibration of alternative theoretical methods? Can theory be used to provide information beyond what is accessible by experiment? With the increasing power of computers, the advance of parallel computing and the development of new theoretical methods, especially time-dependent (TD) calculations of excited states, such questions are becoming increasingly pertinent. We will discuss examples based on the studies described above.

4.1. The Ptpop ion

The Pt—Pt and Pt—P distance changes on excitation resulting from geometry optimization of the excited triplet state and excited-state–ground-state energy differences obtained with the B88P86, B88LYP and PW86LYP density functionals are illustrated in Fig. 14. As is the case for the ground-state Pt—Pt bond length, the magnitude of its shortening upon excitation is very much dependent on both the density functional selected and, in this case, on the treatment of relativistic effects. The B88LYP and B88P86 functionals with the Pauli frozen core predict the largest reduction of the Pt—Pt bond upon excitation ($\Delta = \sim -0.5$ Å). Replacement of the Pauli with the ZORA Hamiltonian (Lenthe *et al.*, 1996) consistently reduces the shortening and leads to better agreement with the experimental value for the Pt—Pt distance shortening shown in green. The blue lines represent the theoretical lengthening of the Pt—P distances, predicted by all calculations. At the time these calculations were published this result was in disagreement with an earlier experiment (Thiel *et al.*, 1993), but it has now been confirmed by recent EXAFS measurements (van der Veen *et al.*, 2009).

The frozen-core PW86LYP results for both the Pt—Pt shortening and the $3A_u$ TD-DFT excitation energy agree well with the experimental information and appear superior to the other methods examined.

4.2. The $[Rh_2(1,8\text{-diisocyano-}p\text{-menthane})_4]^{2+}$ ion

The experimental Rh—Rh contraction of ~0.86 (5) Å on excitation of this ion to its triplet state is the largest geometry change observed in any of our studies (Coppens *et al.*, 2004). Is it reproduced by theory? Two different TD-DFT calculations agree on the shortening of 1.50 Å, even though the ground-state Rh—Rh bond length is poorly reproduced by the two calculations (see Table 1). In both calculations the ZORA relativistic approach was used, as it was found to perform much better in the calculations on the platinum complex. The theoretical shortening considerably exceeds the experimental result, but DFT calculations performed with the *ADF*

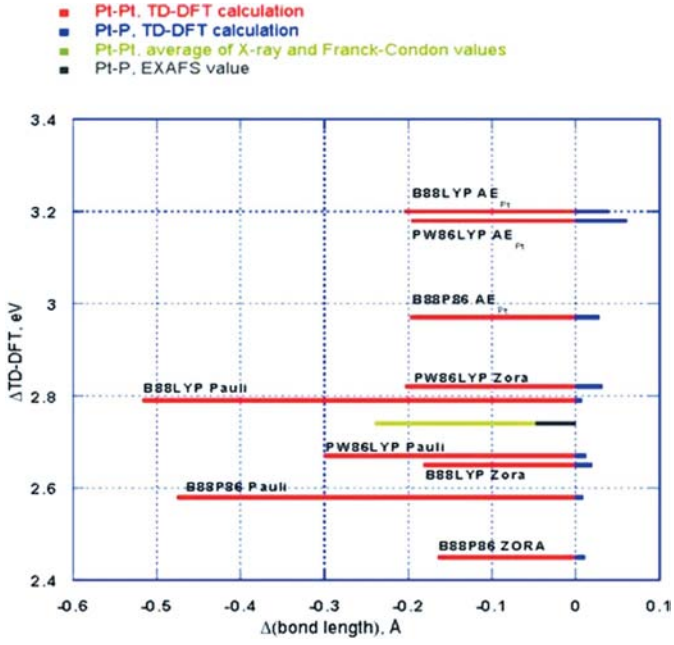

Figure 14
Summary of theoretical and experimental results for Pt—Pt and Pt—P bond-length changes upon ($3d\sigma \rightarrow 4p\sigma$) excitation, and TD-DFT and experimental excitation energies. [Reprinted with permission from Novozhilova *et al.* (2003). Copyright 2003 American Chemical Society.]

Table 1
Ground- and excited-state bond lengths (Å) for the binuclear Rh complex.

	Experiment	TD-DFT BP86 (Turbomole, GTO)	BP86 (ADF, STO)
Rh—Rh ground state	4.496 (1)	4.630	4.553
Rh—Rh triplet state	3.64 (5)	3.14	3.05
Contraction	0.86 (5)	1.49	1.50

program and the BP86 density functional show the potential energy minimum to be shallow as a function of the Rh—Rh bond length (Fig. 15), in agreement with the observed ground-state stretching frequency of only 28 cm^{-1}. According to the theoretical potential curve the shortening corresponds to an excited-state energy difference of only 7.3 kJ, quite small compared with typical bond energies, and likely sensitive to details of the calculations.

The HOMO and LUMO diagrams shown in Fig. 16 illustrate the nature of the excitation from an antibonding to a bonding orbital.

4.3. The Cu 3,5-trifluoromethyl pyrazolate trimer

Since the photo-induced process on excitation in this crystal is intermolecular, calculations were performed on a dimer of trimers, starting with the experimental geometry (Fig. 17). Geometry optimization using different functionals and basis sets leads to quite different results on the ground-state geometry of the dimer. The BLYP and BP86 functionals gave

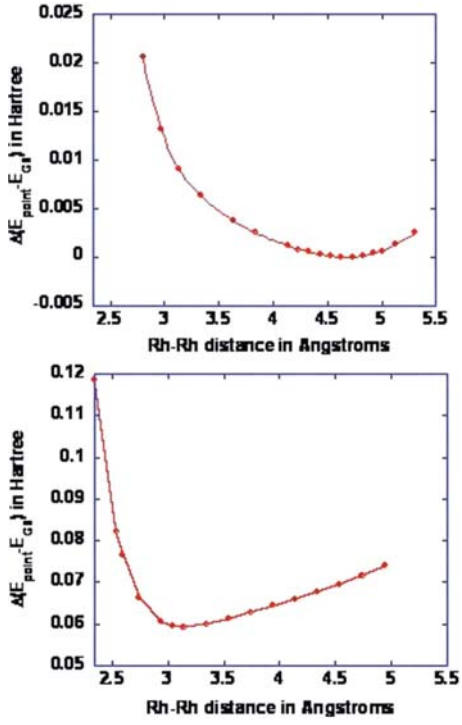

Figure 15
Rh—Rh potential energy curves of the ground state (top) and the first triplet state (bottom) of $[Rh_2(1,8\text{-diisocyano-}p\text{-menthane})_4]^{2+}$ BP86/SV(P). Calculated energy differences between the theoretical-optimized and experimental geometries are 0.37 and 7.3 kJ mol^{-1} for the ground and triplet states, respectively.

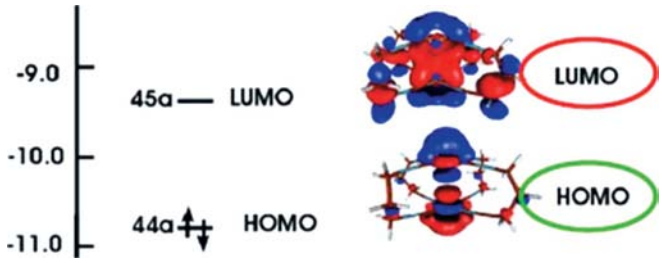

Figure 16
Frontier molecular orbitals of the dinuclear Rh complexes. Isosurface values at 0.03 a.u. for the LUMO, 0.02 a.u. for the HOMO.

the best agreement with the ground-state structure and were selected for the following excited-state calculations. However, while the bond shortening was predicted, the calculations underestimated the observed bond shortening on excitation at a value of 0.30 Å, significantly less than the experimental result of 0.56 Å. An orbital plot of the LUMO shows that on excitation to the A_u level the two interacting Cu atoms in adjacent molecules are linked by a weak $p\sigma$ bond, with contributions from the p orbitals on the adjacent nitrogen atoms (Fig. 18). The HOMO and HOMO-1 have large amplitudes on the two Cu atoms which are not involved in the bond formation, suggesting an intermetallic charge transfer prior to excimer formation.

4.4. Molecular distortion of the photosensitizer dye $[Cu^{I}(dmp)(dppe)][PF_6]$

The overall change of the molecules in the lattice is illustrated in Fig. 19. Following Dobson *et al.* (1984), the conformation of the Cu^{I} diimines can be described in terms of the intramolecular interligand dihedral angle and the rocking and wagging angles of the ligands. The angles θ_x, θ_y and θ_z (Fig. 19) are 90° in the idealized D_{2d} symmetry of the ground-state Cu^{I}

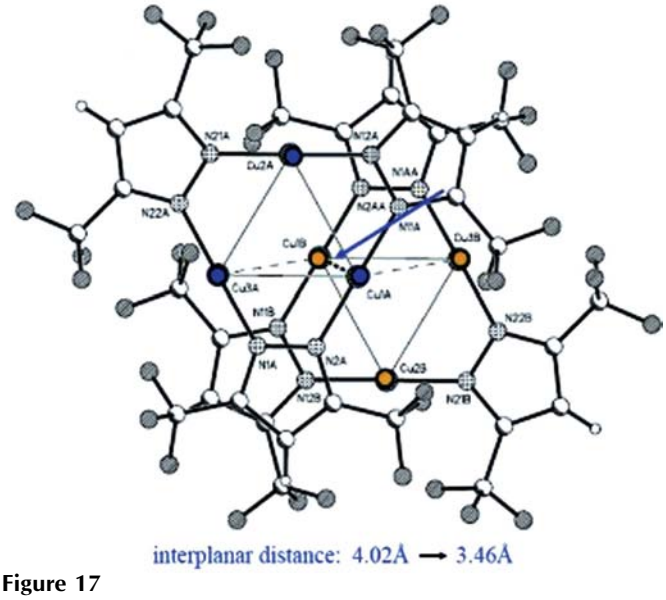

Figure 17
Top view of the Cu pyrazolate trimer, indicating the interplanar Cu—Cu distance (pointed out by the blue arrow) which is shortened on excitation from 4.020 (1) to 3.46 (1) Å.

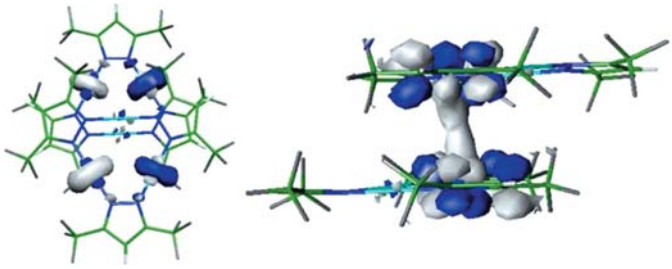

Figure 18
The HOMO seen from above (left) with the bond-forming Cu atoms [Cu(1)] in the center, and the LUMO, seen sideways, of the {[3,5-$(CF_3)_2$Pz]Cu}$_3$ trimer. Surfaces are at an isodensity value of $\pm$0.03 a.u. (Vorontsov *et al.*, 2005).

complexes, but deviate from this value as the distortion from D_{2d} symmetry increases. The experimental values are listed in Table 2 for the ground-state and excited-state structures of both molecules, together with those calculated for both states of $[Cu^I(dmp)(dmpe)]^+$. The deviations of the θ angles from 90° correspond to the rocking, wagging and flattening motions of the molecule.

In both independent molecules in the crystal the rocking distortion $(90 - \theta_x)$ decreases to an absolute value of 0.4 (5)°, not significantly different from zero, in agreement with a decrease from 2.2 to 0.6° calculated with DFT for the isolated $[Cu^I(dmp)(dmpe)]^+$ ion. The wagging distortion, defined by $(90 - \theta_y)$, similarly reduces to very small values in molecule 1 [1.4 (5)°] and in the isolated reference molecule, but essentially remains constant at the non-zero value of ~5° in molecule 2.

The most interesting distortion is the flattening, *i.e.* the deviation of θ_z from 90°, which would correspond to a change from the Cu^I to the Cu^{II} geometry. It is more than 30° in the isolated $[Cu^I(dmp)_2]^+$ complex, and calculated at 8° for the

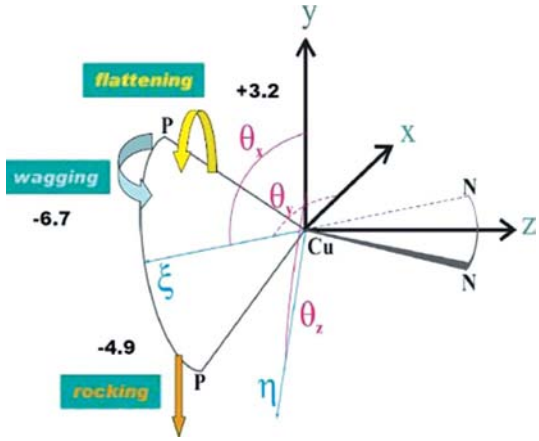

Figure 19
Schematic representation of the distortions of the $[Cu^I(dmp)(diphos)]^+$ complex (molecule 1), with the distortions as defined by Dobson *et al.* (1984) for $Cu(dmp)_2$ complexes. The θ_x and θ_y angles describe the rocking and wagging distortions, and θ_z the flattening distortion. The coordinate system is chosen such that triangle N—Cu—N lies in the *XZ* plane. The unit vector ξ bisects the P—Cu—P angle; the unit vector η is perpendicular to the P—Cu—P plane. [Reprinted with permission from Vorontsov *et al.* (2009). Copyright 2009 American Chemical Society.]

Table 2
Angular distortions on excitation of $[Cu^I(dmp)(dppe)][PF_6]$ according to experiment and theory.

	Ground state	Excited State	Change on excitation
Experiment molecule 1			
θ_x (rocking)	94.5 (1)	89.6 (5)	−4.9
θ_y (wagging)	95.3 (1)	88.6 (5)	−6.7
θ_z (flattening)	90.5 (1)	93.7 (5)	+3.2
Experiment molecule 2			
θ_x	95.6 (1)	90.4 (5)	−5.2
θ_y	84.1 (1)	85.1 (5)	−1.0
θ_z	92.8 (1)	92.7 (5)	−0.1
Theory			
θ_x	92.2	90.6	−1.6
θ_y	91.7	90.1	−1.6
θ_z	93.8	101.8	+8.0

isolated $[Cu^I(dmp)(dmpe)]^+$ ion. The experiment shows the excited-state flattening in the crystal to be only 3.2 (5)° in molecule 1, and no flattening beyond the ground-state value of 2.8° in molecule 2, indicating a significant constraining effect of the crystal lattice. The different behavior of the two independent molecules may be related to the bi-exponential decay of the emission observed at low temperatures (Vorontsov *et al.*, 2009). This explanation is supported by the single-exponential decay of the emission in room-temperature solutions.

4.5. The $[Cu(NH_3)_2]_2^{++}$ cation

DFT calculations with the B3LYP functional show that, unlike the ground state of the isolated molecule, the triplet excited state has a minimum as a function of Cu—Cu bond length at 2.60 Å. This is slightly shorter than the observed excited-state bond length of 2.72 (1) Å, illustrated in Fig. 11, but, given the dependence on computational detail, is in reasonable agreement with experiment.

4.6. The xanthone excimer

DFT calculations of the xanthone dimer showed an unacceptably large dependence of the interplanar distance on the functional and basis set selected for the calculation, with a range of 4.22–3.15 Å. This is perhaps not surprising as dispersion forces are not properly accounted for in DFT. MP2 calculations of the ground state with 6-31G* and 6-31G** basis sets give values of 3.099 and 3.207 Å, respectively, compared with 3.39 Å (16 K) determined experimentally. For the ^3A_u excited state the MP2/6-31G** calculation predicts a contraction of the interplanar spacing of the average molecular planes to 3.144 Å, essentially equal to the experimental value of 3.14 Å (Zheng & Coppens, unpublished results). However, given the large discrepancy between theory and experiment found for the ground state, the significance of this result is uncertain. As pointed out by one of the referees, it is possible that the amount of electron correlation included by the perturbative MP2 treatment could be limited by a not sufficiently flexible basis set. The xanthone molecules in the

excimer are not completely planar, as is clear from Fig. 13; the spacing of the central rings is 0.06 Å less than that of the average molecular planes.

5. Conclusions

Perhaps the most striking conclusion of the comparison between theory and experiment is that, although there is generally at least qualitative agreement, large variations are found between different theoretical approaches. On the other hand, conversion percentages that have been reached in the experiments are often very small, especially when neat crystals are used, limiting the accuracy of the results. Theoretical methods for calculating properties of excited states are improving rapidly, together with further increases in computing power. The above system-by-system comparisons should be followed by a comprehensive study using a broader spectrum of theoretical approaches. In parallel, experimental techniques are benefiting from beamline improvements, development of new sources and changes in data collection techniques. The field is clearly still in an early stage. Single-pulse Laue experiments have so far not produced results of sufficient accuracy for analyses at atomic resolution, but progress is being made, as described above. We can look forward to exciting new results in the coming years.

The authors would like to thank Robert W. Henning for expert assistance at BioCARS beamline 14-ID and the referees for helpful comments. This work was funded by the Division of Chemical Sciences, Geosciences, and Biosciences, Office of Basic Energy Sciences of the US Department of Energy through Grant DEFG02-ER15372. Use of the Advanced Photon Source was supported by the US Department of Energy, Basic Energy Sciences, Office of Science, under Contract No. DE-AC02-06CH11357. Use of the BioCARS Sector 14 was supported by the National Institutes of Health, National Center for Research Resources, under grant number RR007707. Time-resolved set-up at Sector 14 was funded in part through a collaboration with Philip Anfinrud (NIH/NIDDK). The ChemMatCars15-ID beamline is funded by the National Science Foundation (CHE0087817).

References

Abdelmoty, I., Buchholz, V., Di, L., Guo, C., Kowitz, K., Enkelmann, V., Wegner, G. & Foxman, B. M. (2005). *Cryst. Growth Des.* **5**, 2210–2217.

Benedict, J. B. & Coppens, P. (2009). *J. Phys. Chem.* **113**, 3116–3120.

Bessho, T., Constable, E. C., Graetzel, M., Redondo, A. H., Housecroft, C. E., Kylberg, W., Nazeeruddin, M. K., Neuburger, M. & Schaffner, S. (2008). *Chem. Commun.* pp. 3717–3719.

Bolotovsky, R. & Coppens, P. (1997). *J. Appl. Cryst.* **30**, 244–253.

Carvajal, M. A., Alvarez, S. & Novoa, J. J. (2004). *Chem. Eur. J.* **10**, 2117–2132.

Christensen, M., Haldrup, K., Bechgaard, K., Feidenhans'l, R., Kong, Q., Cammarata, M., Russo, M. L., Wulff, M., Harrit, N. & Nielsen, M. M. (2009). *J. Am. Chem. Soc.* **131**, 502–508.

Coppens, P., Gerlits, O., Vorontsov, I. I., Kovalevsky, A. Y., Chen, Y.-S., Graber, T. & Novozhilova, I. V. (2004). *Chem. Commun.* pp. 2144–2145.

Coppens, P., Pitak, M., Gembicky, M., Messerschmidt, M., Scheins, S., Benedict, J., Adachi, S., Sato, T., Nozawa, S., Ichiyanagi, K., Chollet, M. & Koshihara, S. (2009). *J. Synchrotron Rad.* **16**, 226–230.

Coppens, P., Vorontsov, I. I., Graber, T., Gembicky, M. & Kovalevsky, A. Y. (2005). *Acta Cryst.* A**61**, 162–172.

Coppens, P., Zheng, S.-L., Gembicky, M., Messerschmidt, M. & Dominiak, P. M. (2006). *Cryst. Eng. Commun.* **8**, 735–741.

Dobson, J. F., Green, B. E., Healy, P. C., Kennard, C. H. L., Pakawatchai, C. & White, A. H. (1984). *Aust. J. Chem.* **37**, 649–659.

East, A. L. L. & Lim, E. C. (2000). *J. Chem. Phys.* **113**, 8981–8994.

Enkelmann, V. & Wegner, G. (1993). *J. Am. Chem. Soc.* **115**, 10390–10391.

Forster, T. (1965). *Excimers and Exciplexes*, Vol. 3, *Modern Quantum Chemistry*, edited by O. Sinanoglu, pp. 1–21. New York: Academic Press.

Forster, T. & Kasper, K. (1954). *Z. Phys. Chem. NF*, **1**, 275.

Gembicky, M. & Coppens, P. (2007). *J. Synchrotron Rad.* **14**, 133–137.

Graber, T., Henning, R. W., Kosheleva, I., Ren, Z., Srajer, V., Moffat, K., Cho, H.-S., Dashdorj, N., Schotte, F. & Anfinrud, P. (2009). *Annual Meeting of the American Crystallographic Association*, Abstract 6.10.12, Toronto, Canada.

Guo, W., Yang, B., Wang, C.-X., Harkay, K. & Borland, M. (2007). *Phys. Rev. ST Accel. Beams*, **10**, 020701.

Helliwell, J. R., Habash, J., Cruickshank, D. W. J., Harding, M. M., Greenhough, T. J., Campbell, J. W., Clifton, I. J., Elder, M., Machin, P. A., Papiz, M. Z. & Zurek, S. (1989). *J. Appl. Cryst.* **22**, 483–497.

Kazimirov, A., Smilgies, D.-M., Shen, Q., Xiao, X., Hao, Q., Fontes, E., Bilderback, D. H., Gruner, S. M., Platonov, Y. & Martynov, V. V. (2006). *J. Synchrotron Rad.* **13**, 204–210.

Kim, C. D., Pillet, S., Wu, G., Fullagar, W. K. & Coppens, P. (2002). *Acta Cryst.* A**58**, 133–137.

Lenthe, E. V., Leeuwen, R. V., Baerends, E. J. & Snijders, J. G. (1996). *Int. J. Quant. Chem.* **57**, 281–293.

Leung, K. H., Phillips, D. L., Che, C.-M. & Miskowski, V. M. (1999). *J. Raman Spectrosc.* **30**, 987–993.

Lim, E. C. (1987). *Acc. Chem. Res.* **20**, 8–17.

Lim, E. C. (2002). *Res. Chem. Intermed.* **28**, 779–794.

Lim, E. C., Locke, R. J., Lim, B. T., Fujioka, T. & Iwamura, H. (1987). *J. Phys. Chem.* **91**, 1298–1300.

Ma, B.-Q. & Coppens, P. (2003). *J. Org. Chem.* **68**, 9467–9472.

Messerschmidt, M. & Tschentscher, T. (2008). *Acta Cryst.* A**64**, C611.

Novozhilova, I., Volkov, A. V. & Coppens, P. (2003). *J. Am. Chem. Soc.* **125**, 1079–1087.

Ozawa, Y., Terashima, M., Mitsumi, M., Toriumi, K., Yasuda, N., Uekusa, H. & Ohashi, Y. (2003). *Chem. Lett.* **32**, 62–63.

Ren, Z. & Moffat, K. (1995). *J. Appl. Cryst.* **28**, 461–481.

Rice, S. F. & Gray, H. B. (1983). *J. Am. Chem. Soc.* **105**, 4511–4515.

Schoenlein, R. W., Chattopadhyay, S., Chong, H. H. W., Glover, T. E., Heimann, P. A., Shank, C. V., Zholents, A. A. & Zolotorev, M. S. (2000). *Science*, **287**, 2237–2240.

Thiel, D. J., Livins, P., Stern, E. A. & Lewis, A. (1993). *Nature (London)*, **362**, 40–43.

Veen, R. M. van der, Milne, C. J., El Nahhas, A., Lima, F. A., Pham, V.-T., Weinstein, J., Borca, C. N., Abela, R., Bressler, C. & Chergui, M. (2009). *Angew. Chem. Int. Ed.* **48**, 2711–2714.

Vorontsov, I. I. & Coppens, P. (2005). *J. Synchrotron Rad.* **12**, 488–493.

Vorontsov, I., Graber, T., Kovalevsky, A., Novozhilova, I., Gembicky, M., Chen, Y.-S. & Coppens, P. (2009). *J. Am. Chem. Soc.* **131**, 6566–6573.

Vorontsov, I. I., Kovalevsky, A. Y., Chen, Y.-S., Graber, T., Gembicky, M., Novozhilova, I. V., Omary, M. A. & Coppens, P. (2005). *Phys. Rev. Lett.* **94**, 193003.

Zheng, S.-L. & Coppens, P. (2005*a*). *Cryst. Growth Des.* **5**, 2050–2059.

Zheng, S.-L. & Coppens, P. (2005*b*). *Chem. Eur. J.* **11**, 3583–3590.

Zheng, S.-L., Gembicky, M., Messerschmidt, M., Dominiak, P. M. & Coppens, P. (2006). *Inorg. Chem.* **45**, 9281–9289.

Zheng, S.-L., Messerschmidt, M. & Coppens, P. (2005). *Angew. Chem. Int. Ed.* **44**, 4614–4617.